Intervention timing of H* and •OH determines the catalytical degradation of tribromophenol by palladium(II) doped green rust in redox-alternating environments

Xuejie Zhang [a,b], Qianqian Jia [a,b], Jia Deng [a,b], Lili Li [c], Yitao Dai [d], Liandong Zhu [e], Li-Zhi Huang [a,b,*]

[a] School of Civil Engineering, Wuhan University, No. 8, East Lake South Road, Wuhan 430072, PR China
[b] State Key Laboratory of Water Resources and Hydropower Engineering Science, Wuhan University, 430072, PR China
[c] Central Laboratory, Renmin Hospital of Wuhan University, Wuhan 430060, PR China
[d] Department of Applied Chemistry, University of Science and Technology of China, Hefei 230026, PR China
[e] School of Resources & Environmental Science, Hubei International Scientific and Technological Cooperation Base of Sustainable Resource and Energy, Hubei Key Laboratory of Biomass-Resources Chemistry and Environmental Biotechnology, Wuhan University, Wuhan 430079, PR China

ARTICLE INFO

ABSTRACT

Atomic hydrogen (H*) and hydroxyl radicals (•OH) can synergistically realize efficient mineralization of halogenated organic pollutants, but it requires an electrocatalytic or photoelectrocatalytic system. In this work, we developed a simple synergetic reduction-oxidation system for the degradation of tribromophenol (TBP) using Pd (II) doped green rust (GR). GR reduced Pd(II) to Pd(0) which catalyzed H_2O/H^+ to produce H* . H* completely reduced TBP to phenol. Meanwhile, excess H* involved in the generation of •OH under oxic conditions. The synergistic involvement of H* and •OH realized the mineralization of TBP, which could not be achieved by H* or •OH alone. Furthermore, the diffusion rate of dioxygen into solution determined sequential or synchronous involvement of H* and •OH, which significantly affected the mineralization efficiency of TBP. We proposed that the most efficient way to mineralize TBP was initiating H*-involved nucleophilic hydrodebromination first and then initiating •OH-involved electrophilic oxidation.

1. Introduction

Atomic hydrogen (H*, $E_0 = -2.1$ V vs RHE) and hydroxyl radical (•OH, $E_0 = 2.8$ V vs RHE) are highly active reducing and oxidizing species, respectively [1–4]. H* was always generated by the electro-catalytic processes of metals such as Ni, Pd, and Ag, and the proton (H^+) in aqueous solution was reduced to H* on the cathode surface [5–7]. H* was often used for hydrodehalogenation reactions to achieve complete dehalogenation of halogenated compounds [8,9]. However, H* alone could not realize the final ring-opening and mineralization of refractory organic compounds such as halogenated aromatic hydrocarbons (HAHs) [10,11]. •OH, as the strongest reactive oxygen species (ROS) in the environment, can non-selectively oxidize most organic pollutants and redox-sensitive elements [12–14]. Advanced oxidation process based on hydroxyl radical is an effective technology to degrade and mineralize persistent organic pollutants, especially organic pollutants with aromatic rings. Due to its high redox potential, •OH can achieve ring opening and mineralization of the benzene ring [15], which is difficult to achieve by other oxidation approaches. However, the generation of more toxic halogenated aromatic intermediates hinders the application of HAHs removal technology using •OH alone [15]. Therefore, it is necessary to reduce the toxicity of HAHs by synergistic reduction and oxidation technology. The redox synergy between H* and •OH can realize efficient mineralization of persistent refractory organics [16–18]. However, the latest research all used electrocatalytic (EC) and photo-electrocatalytic (PEC) systems [18,19], in which H* was generated by catalysis of Pd-loaded cathode and •OH was generated by the dioxygen activation in the solution. Although these processes could introduce H* and •OH into the same reaction system, they have high requirements for electrode fabrication and require the energy input of electricity and/or light. Moreover, previous studies only verified that the synergistic effect of H* and •OH on halogenated compounds removal was more effective

* Corresponding author at: School of Civil Engineering, Wuhan University, No. 8, East Lake South Road, Wuhan 430072, PR China.
E-mail address: lizhihuang@whu.edu.cn (L.-Z. Huang).

than that of single component, but ignored the importance of the initiation sequence of redox reaction by H* and ●OH. The different timing of H* and ●OH intervening in the reaction would lead to different dehalogenation degrees and hydroxylation degrees of intermediate products, and finally lead to different mineralization degrees of halogenated compounds [20]. In the natural underground environment, oxygen concentration gradually changes from high to low with the transition from soil to sediment [21]. However, the effect of different oxygen content on the reduction or oxidation sequence of halogenates has never been reported. Furthermore, excessive exploitation of groundwater and seasonal changes would also cause the fluctuation of groundwater level, resulting in the alternating anoxic and oxic environment of groundwater [22–24], which would have unknown effects on the redox synergistic degradation of halogenated compounds.

GR is one of the most active iron-bearing minerals found in iron-rich anoxic sediments, soils and aquifer systems [25,26]. GR was often used in bimetallic catalytic reduction dehalogenation reactions [27,28], and GR has the potential to reduce Pd(II) to Pd(0). Pd(0) is the most favorable catalyst for H* generation and the surface of Pd(0) can efficiently retain H*[29,30]. In addition, GR can activate dioxygen to produce ●OH, which has been confirmed in our previous studies [31–33]. Therefore, it is possible to realize the synergistic involvement of H* and ●OH in the same system by adding Pd(II) to GR, but this process has not been studied before. Compared with the previous research on EC and PEC, the experimental design and method of our study are simpler and easier to operate, and do not require additional energy. In addition, the sequence of H* or ●OH intervention is regulated by changing the experimental environments (anoxic, oxic, and the rate of oxidation). Then, the influence of H* or ●OH intervention sequence on the mineralization of HAHs is investigated, which has not been studied in previous experiments.

Tribromophenol (TBP) is a persistent HAHs, which is used as the target contaminant in this work. TBP, as an intermediate of flame retardant, has a low natural attenuation rate and has been found in subsurface environments, including soil, sediment and groundwater [34,35]. TBP is highly toxic, carcinogenic, and has adverse effects on the thyroid hormone system in animals and humans [36]. The stable C-Br bonds in TBP are the reason for its toxicity and persistence, and debromination with the breakage of the C-Br bonds is essential to detoxify TBP [37]. While, phenol, as the complete debromination product of TBP, is still toxic, so the mineralization of TBP is the key for its complete detoxification. In this paper, the Pd(II) doped green rust (GR-Pd(II)) was used to achieve the co-production of H* and ●OH in the reaction system and the synergistic degradation of TBP by H* and ●OH without the input of external energy. We propose a novel coexistence system of H* and ●OH by mixing GR with Pd(II), in which the reducibility of GR to transition metals and the catalysis of Pd(0) to generate H* were fully utilized. We aim to (a) evaluate the redox synergistic effects of H* and ●OH on the mineralization of TBP, (b) reveal the advantages of synergetic H* reduction with ●OH oxidation compared with single component, and (c) explore the influence of the synchronous or sequential involvement of H* and ●OH on the degradation pathway and mineralization efficiency of TBP.

2. Materials and methods

2.1. Chemicals

The synthesis of GR was the same as previously reported (Text S1) [38]. The dosage of GR in the experiments was determined by the Fe(II) concentration of GR (Fe(II)$_{GR}$). Details of the other chemicals are described in Text S2.

2.2. The experiments under anoxic, oxic and anoxic-to-oxic conditions

In the anoxic experiment, the sample was prepared in a glovebox, and the reaction solution was prepared in 100 mL airtight glass vials.

TBP and PdCl$_2$ were added first, and the pH was adjusted to 8 before the addition of GR to avoid the acidic decomposition of GR. Finally, the pH was adjusted to 8 again. The total reaction solution was 50 mL, and the headspace of reaction vials was N$_2$. The vials were wrapped in tin foil after sealing to avoid any potential photochemical reactions and the reaction was initiated by magnetically stirring the reaction suspensions at 550 rpm in the glovebox.

In order to regulate the intervention timing of H* or ●OH and verify its influence on TBP degradation, two types of oxic experiments were performed: (a) the reaction vial was open (fast oxidation experiment) and (b) the reaction vial was sealed but the headspace was filled with air (slow oxidation experiment). The preparation process is the same as that under anoxic conditions, except that reaction vials were taken out of the glovebox during the reaction. The change of dissolved oxygen (DO) in solution was monitored by a dissolved oxygen meter. 10 mM benzoic acid was used as a probe to capture ●OH in oxic experiments. The effects of H* or ●OH at different time periods were verified by quenching experiments with different gradients of tertiary butanol (TBA). At the predetermined interval, ~1 mL of suspension was removed and immediately filtered through a 0.22 μm PTFE filter to analyze the concentrations of p-hydroxybenzoic acid (p-HBA), TBP and the intermediate products of TBP.

The anoxic-to-oxic experiment was conducted to achieve a strict sequential reduction-oxidation reaction. The reaction vials were first magnetically stirred in the glovebox for 1 h, then removed from the glovebox, and magnetically stirred outside the glovebox with an air headspace for 4 h. All the experiments were carried out at least in duplicate.

2.3. Analytical methods and characterizations

The variation of TBP and its intermediate products, bromine ions, ●OH concentrations were determined and the analysis details were shown in Text S3. High-performance liquid chromatography-mass spectrometry (HPLC-MS, Agilent Technologies) was employed to analyze the oxidative intermediates of TBP. The H$_2$ generated from H* during the anoxic reaction of GR-Pd(II) was collected using a gas-tight syringe and monitored by a gas chromatograph (GC2010, Shimadzu, Japan). Fe(II) and Fe(III) in the GR were determined by a modified phenanthroline spectrophotometric method (Text S4) [39]. The mineralogical changes of GR after anoxic or oxic reaction were characterized by X-ray diffraction (XRD) using a Malvern X-ray diffractometer (XPert Pro). The valence and content of Fe and Pd on the mineral surface were determined by XPS using a Kratos Axis Ultra^{DLD} instrument. In order to observe surface morphologies and internal structures of the GR-Pd(II) sample, the GR-Pd(II) was analyzed by scanning electron microscopy (SEM, ZEISS Gemini 300), transmission electron microscopy (TEM, JEM-F200) and scanning transmission electron microscopy equipped with an energy-dispersive X-ray spectroscopy detector (STEM-EDS, JED-2300 T, Japan). Fourier transform infrared (FTIR, Thermo Scientific Nicolet iS20) and Raman (HORIBA Scientific LabRAM HR Evolution) spectroscopy were employed to characterize molecular structure information of GR and GR-Pd(II). The sample for characterizations was put into a vacuum bag and sealed by the vacuum sealing machine in the glovebox to avoid oxidation during sample transfer. The change of total organic carbon (TOC) was monitored by a TOC/TN analyzer (multi N/C 2100, Analytik Jena, Germany). Signals of free radical were determined by electron paramagnetic resonance spectroscopy (EPR) (JES-FA200, JEOL Co., Japan) using 5,5-dimethyl-1-pyrrolidine N-oxide (DMPO) as a spin-trap reagent. The concentration of H$_2$O$_2$ was detected by UV–vis spectrophotometry. TiOSO$_4$/H$_2$SO$_4$ reagent was used as the chromogenic reagent, and the detection wavelength was 400 nm. Electrochemical analyses were performed on an electrochemical workstation (CHI 600E, CH Instruments, USA). The details of the electrochemical experiments, including open-circuit potential curve (OCPT), electrochemical impedance spectroscopy (EIS), cyclic voltammetry (CV) and

Tafel curves, are shown in Text S5.

2.4. Density functional theory (DFT) calculation analysis

The fitted electrostatic potential (ESP) charge and condensed Fukui function were calculated to predict nucleophilic and electrophilic reaction sites of TBP and its oxidation/reduction products. The structural optimization, free energy change of TBP degradation and electron spin density of the intermediates were also calculated. Details on DFT calculation are shown in Text S6.

3. Results and discussion

3.1. GR-Pd(II) characterization

Fig. 1 depicts the SEM, TEM images and STEM-EDS spectra of the GR-Pd(II) sample. SEM and TEM images showed that GR has a characteristic hexagonal morphology (Fig. 1a-b). STEM-EDS afforded elemental analysis and confirmed the existence of trace Pd in the sample (Fig. 1c). EDS maps clearly revealed the presence of Pd in the hexagonal plates and the near-homogeneous distribution of Fe, O, and Pd across the GR crystal (Fig. 1d). XPS data showed that 100% of Pd existed in the form of Pd(0) (Fig. 2b, Table S1), demonstrating that GR can reduce all Pd(II) to Pd(0). The FTIR spectrum showed that GR has O-H stretching at 3408 cm^{-1}, H_2O deformation at 1624 cm^{-1}, and Fe-OH deformation at 850 and 669 cm^{-1} (Fig. 2c) [40]. The Raman spectrum showed two characteristic peaks of GR at 438 and 501 cm^{-1} (Fig. 2d), which were attributed to Fe^{2+}–OH and Fe^{3+}–OH stretching, respectively [41]. The weak peaks at 609 and 617 cm^{-1} were attributed to hematite [42], which may be due to the inevitable oxidation of GR during the analysis process. The FTIR and Raman spectra of GR-Pd(II) are the same as that of GR, suggesting that Pd(II) was reduced to Pd(0) by GR without bond formation. Pd(0) may be distributed on the GR surface in the form of polyatomic clusters.

3.2. Degradation of TBP by H* or •OH alone

In order to compare the influence of single radicals (H* or •OH), two experimental environments were designed. One is the reaction of GR-Pd (II) under anoxic conditions, which only has the active component of H* . The other is the reaction of GR alone under oxic conditions, which only has the active component of •OH.

Under anoxic conditions, TBP was rapidly debrominated to phenol in the GR-Pd(II) system. The degradation efficiency reached 97% in 5 min and 100% in 15 min (Fig. 3a). No reduction products except phenol were detected, indicating that TBP debromination process was rapid and thorough. In contrast, GR alone had no reduction but only adsorption effect on TBP (Fig. 3b), which was also confirmed in our previous study [33]. Therefore, the addition of Pd(II) is the key to the reduction of TBP. GR alone could not transfer electrons to TBP, but the addition of Pd(II) rapidly promoted the flow of electrons to TBP and induced the reduction of TBP.

Pd(0) is an efficient catalyst for catalyzing H_2O/H^+ to form H* . The evolution of H* on Pd(0) surface can be studied by electrochemical analysis. CV curves showed an oxidation peak in the potential ranges of − 0.40 to − 0.20 V corresponding to the oxidation peak of H* in GR-Pd (II) system (Fig. S1a) [10] while no oxidation peak was in GR system (Fig. S1b), which indicated that Pd(0) could transfer electrons to the aqueous solution to generate H* . The oxidation peak of H* disappeared once TBP was added to the electrolyte (Fig. S1b), demonstrating that H* had reacted with TBP and H* replaced the bromine atom in TBP. In addition, H* could also combine into dihydrogen (H_2) via a Heyrovsky or Tafel step [10,43]. To further verify the presence of H* , the amount of H_2 generated in the GR-Pd(II) system in the anoxic environment was detected (Fig. 3c). It can be seen that H_2 was continuously produced during 1 h of the reaction between GR and Pd(II) and reached 75 μM at 1 h. In contrast, GR alone did not produce H_2 (Fig. 3d), which further indicated that the Pd(0) was the active site for producing H* . The accumulation amount of H_2 was only 27 μM after 1 h with the addition of TBP, confirming that the TBP reduction process consumed H* . Furthermore, TBA as an H* scavenger was introduced into the reaction solution (Fig. S2). It was found that the addition of TBA inhibited the production of the reduction product phenol, and the yield of phenol gradually decreased with the increase of TBA concentration. The addition of 1 M TBA reduced the yield of phenol by 30%. The production of phenol was not completely inhibited, indicating that the reduction of TBP was not only due to the hydrogenation reaction induced by H* , but
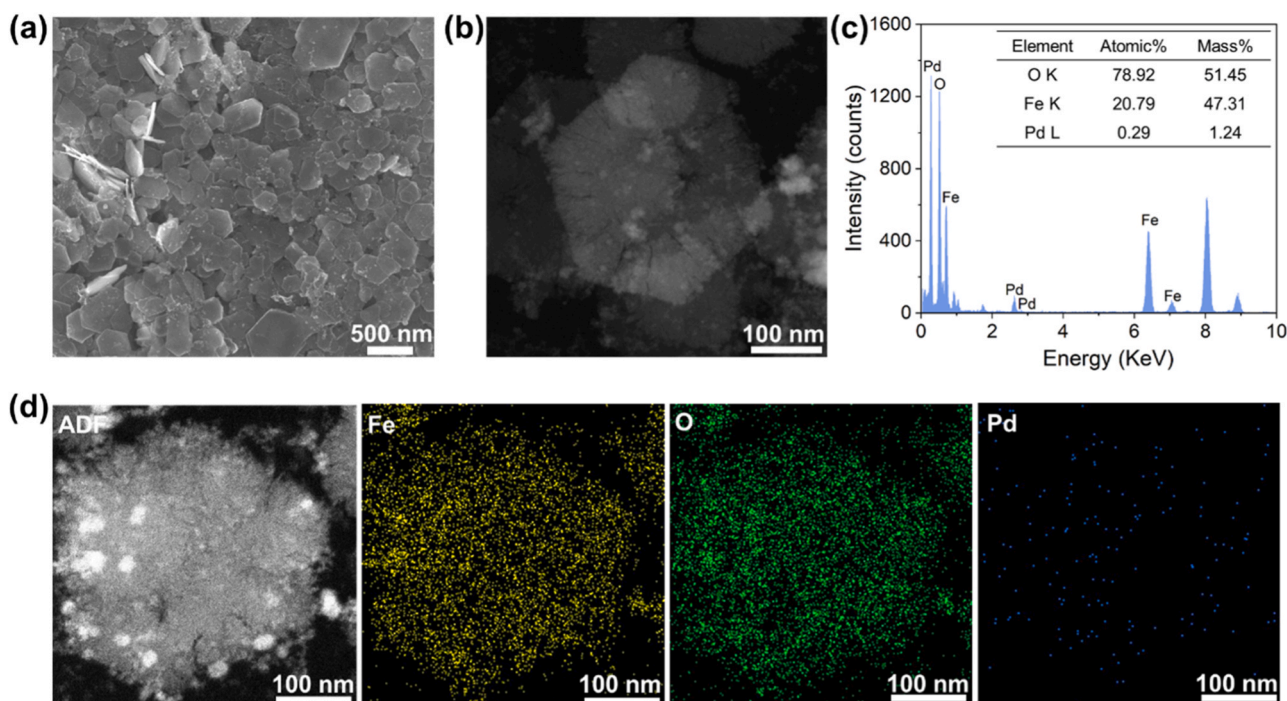

Fig. 1. (a) SEM image, (b) TEM image and (c) STEM-EDS spectra of GR-Pd(II) and (d) the corresponding EDS elemental maps.
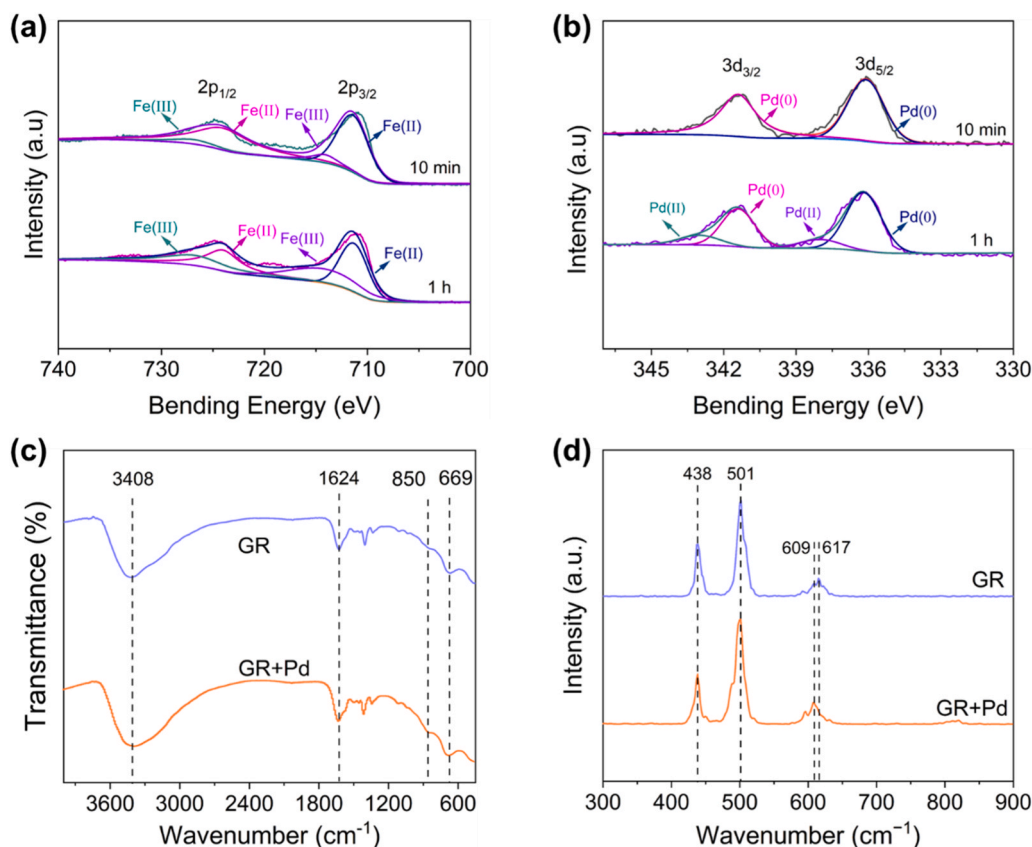
Fig. 2. (a) Fe 2p XPS and (b) Pd 2d XPS under anoxic conditions. (c) FTIR and (d) Raman spectra of GR and GR-Pd(II).

also the direct electron transfer via the galvanic couple effect between the GR and Pd(II). The OCPT/EIS/Tafel curves were also obtained (Fig. S1c-e). The OCPT of GR-Pd(II) was more negative than GR, indicating that GR-Pd(II) was more unstable and more likely to react compared with GR. EIS reflects the interfacial electron transfer rates of different reactants. The smaller arc radius for GR-Pd(II) in EIS compared with GR further demonstrated that the addition of Pd(II) accelerated the electron transfer efficiency of GR, and the increase in the arc radius after the addition of TBP indicated that TBP consumed the transferred electrons. The corrosion currents were obtained by fitting the Tafel curves (Table S2). The corrosion current of GR-Pd(II) (7.531×10^{-7}) was higher than that of GR (6.839×10^{-7}) and decreased after TBP was added (7.092×10^{-7}), which indicated that TBP consumed electrons, resulting in the decrease of electron transfer activity of GR-Pd(II) system. Although GR-Pd(II) has a great reducing activity for TBP and TBP could be rapidly degraded to phenol, phenol could not be further reduced under reducing conditions. Therefore, the mineralization of TBP was not realized by H* alone.

Under oxic conditions, GR could activate dioxygen to produce •OH, and the oxidation rate would directly affect the oxidation of GR [44]. As seen in Fig. 4a, for the fast oxidation experiment, the DO concentration of the reaction solution was relatively low in the first 10 min, but increased rapidly from 10 min (0.2 mg/L) to 20 min (4.9 mg/L) and reached complete saturation in 1 h, which would lead to the rapid oxidation of GR. The oxidative degradation of TBP by GR occurred in the first 1 h, and TBP was not continuously degraded during 1–5 h (Fig. 4b), which was due to that Fe(II) of GR was fully oxidized with the rapid entry of dioxygen into the solution in the first 1 h and could not continuously activate dioxygen. For the slow oxidation experiment, the DO in the reaction solution increased slowly (Fig. 4a). The concentration of DO only reached 0.26 mg/L in 1 h, and did not reach saturation in 5 h. The ferrous iron in GR underwent a slow oxidation process rather

than being rapidly consumed, so GR could continuously activate dioxygen to degrade TBP during the 5 h reaction. Although TBP could be degraded by •OH oxidation under oxic conditions, the degradation efficiency was not high. TBP degradation efficiency was 61% and 40% within 5 h for slow and fast oxidation respectively, which was also confirmed by debromination efficiency. The Br^- produced by the slow and rapid oxidation of TBP for 5 h were 12.3 and 8.3 µM (Fig. 4c), corresponding to 41.7% and 27.8% debromination efficiency, respectively. TOC was basically unchanged in either slow or rapid oxidation process of GR (Fig. 4d), indicating that mineralization of TBP could not be realized by •OH alone. Therefore, synergetic H* reduction with •OH oxidation is required to achieve the mineralization and detoxification of TBP.

3.3. Degradation of TBP by synergistic involvement of H* and •OH

Under oxic conditions, TBP was rapidly degraded by either slow or fast oxidation of GR-Pd(II) (Fig. 5a-b), which was different from the low removal efficiency of TBP by GR alone. During the fast oxidation of GR-Pd(II) system, the degradation efficiency of TBP reached 81% in 15 min, and then the degradation rates of TBP slowed down (Fig. 5a). Reduction products such as 2,4-DBP, 4-BP and phenol were also detected using HPLC. The concentration of 2,4-DBP and phenol increased to 0.69 and 1.58 µM respectively within 30 min and then decreased slowly, while the concentration of 4-BP first increased to a peak value of 1.47 µM at 15 min and then dropped gradually (Fig. 5a). The reduction intermediates were detected during the fast oxidation process, meaning that H* still initiated the reduction reaction in this environment. However, different from the single reduction process, the concentration of reduction product phenol was much lower. Furthermore, The carbon balance consisting of TBP and its reduction products dropped greatly, which indicated that TBP also underwent oxidative degradation.
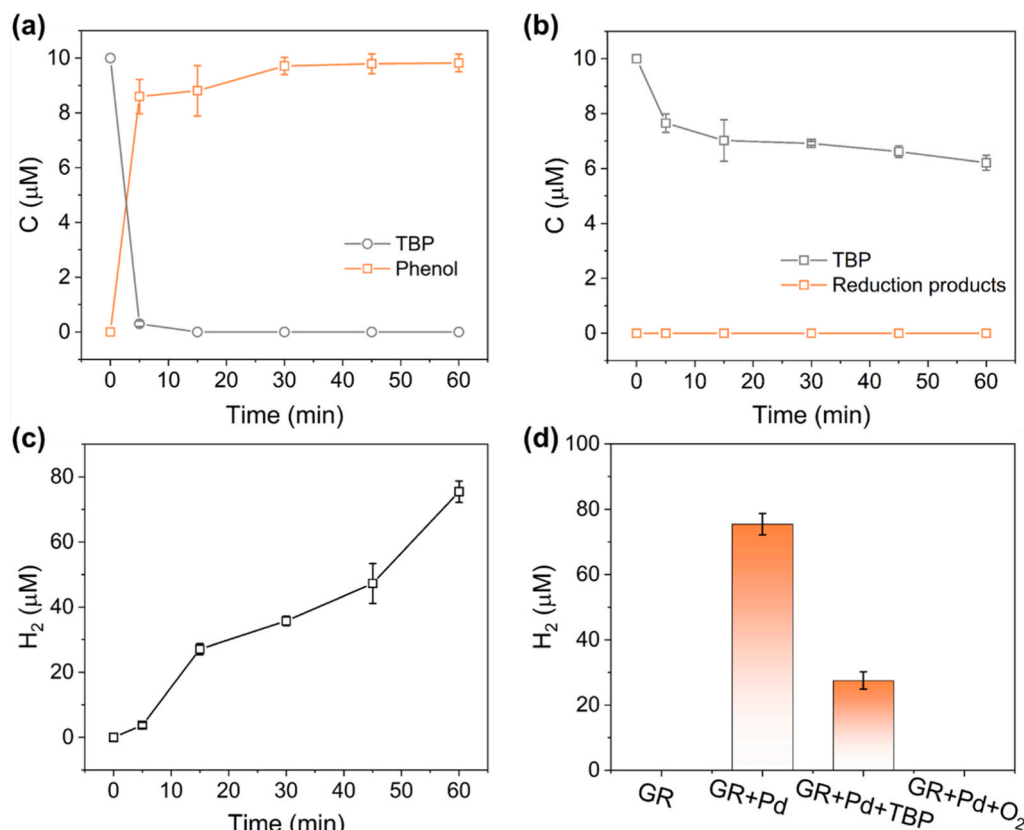
Fig. 3. The removal of TBP by (a) GR-Pd(II) and (b) GR under anoxic conditions. (c) The production of H_2 vs. time in GR-Pd(II) system under anoxic conditions. (d) The production of H_2 under different conditions after 1 h of reaction. Experimental conditions: $[Fe(II)_{GR}] = 10$ mM, $[Pd(II)] = 40$ μM, $[TBP] = 10$ μM, and initial pH = 8.

Hydroxylation products, such as dibromohydroquinone and mono-bromohydroquinone, were detected by LC-MS (Fig. S6a), which were the results of a synchronous attack of H* and •OH [20]. The coexistence of reduction products and oxidation products indicated that the GR-Pd (II) system could realize a synchronous redox process under air conditions. However, due to the rapid entry of dioxygen into the reaction solution, dioxygen as an electron acceptor significantly inhibited the reductive debromination of TBP, resulting in the formation of some incomplete debromination products. During the slow oxidation process, TBP concentration rapidly dropped to 0 in the first 0.5 h, and the yield of the reduction product phenol was ~9.2 μM (Fig. 5b), indicating that hydrodebromination reaction was dominant due to the low DO at the initial stage of reaction. Then, the phenol gradually decreased, but the reduction products of phenol were not found. In contrast, the oxidation products of phenol (e.g. p-phenol and the ring-opening organic acid) were detected using LC-MS (Fig. S6b), which indicated that phenol was oxidized with the gradual increase of DO in the later stage. The complete reductive debromination of TBP was achieved by the slow oxidation process although under oxic conditions, which was due to the high reducibility of H* and its high reactivity with TBP. Moreover, because of the synergistic involvement of •OH in the later stage, phenol could be further degraded, which was not achieved by the reduction of H* alone.

The comparison of the production of •OH in these two oxidation environments was shown in Fig. 5c. In the fast oxidation process, •OH was rapidly generated to 7.5 μM in the first 0.5 h, and then increased slowly, with an accumulation of 11.6 μM at 5 h. The rapid production of •OH and involvement in the reaction system were accountable for the limited reduction products of TBP in this environment. H* and •OH synchronously involved in the early stage of the degradation process, resulting in the simultaneous reduction and hydroxylation of TBP. By contrast, the cumulative concentration of •OH increased slowly to

1.9 μM in the first 0.5 h of the slow oxidation process, and increased continuously during the subsequent oxidation process to 20.7 μM after 5 h of reaction. The generation of •OH under fast or slow oxidation processes was greatly influenced by the change of DO in the reaction solution (Fig. 4a), further confirming that an optimum oxidation rate of GR affected its ability to activate dioxygen. In addition, the low DO in the first 0.5 h of the slow oxidation process also provided reducing environment for the reduction of TBP. Although the small amount of dioxygen in the early stage of the slow oxidation process would consume H*, it had no obvious effect on the reduction of TBP. Because the H* production by GR-Pd(II) was rapid and sufficient (Fig. 3c), H* rapidly initiated the complete debromination of TBP in the first 0.5 h of the slow oxidation process. Subsequently, the continuous increase of •OH in the later stage provided the driving force for the oxidative degradation of phenol.

XPS results revealed that all Pd(II) was reduced to Pd(0) by GR within 10 min in the slow oxidation process, while in the fast oxidation process, only 78.4% of Pd(II) was reduced (Fig. S3, Table S1). The presence of Pd(0) offered the possibility for H* generation and its synergistic participation in the reaction under oxic conditions. Compared with the slow oxidation process, most of Fe(II) was rapidly oxidized into Fe(III) in the first 1 h of the fast oxidation process, indicating that the main redox reaction process occurred in the early stage and the reactivity of GR-Pd(II) was significantly attenuated after the rapid oxidation of Fe(II). It was consistent with the degradation results of TBP under the fast oxidation process. During the slow oxidation process, the content of Fe(II) was 76.0%, 73.7% and 63.2% at 10 min, 1 h and 5 h, respectively, indicating that Fe(II) was in a continuous oxidation process within 5 h. Meanwhile, the oxidation rate also affected the structural transformation of GR under oxic conditions [44,45]. XRD data showed that GR was transformed into lepidocrocite after the fast oxidation reaction,
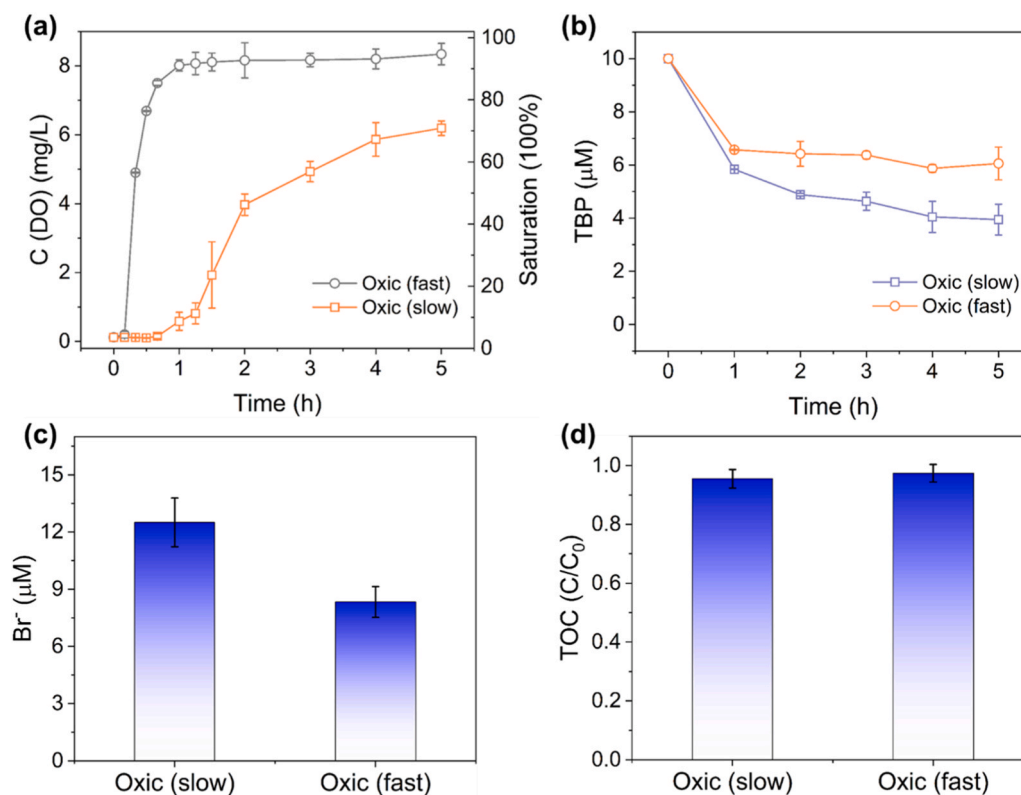
Fig. 4. (a) The change of DO in reaction solution, (b) the removal of TBP, (c) the production of Br$^-$ and (d) the change of TOC in the fast and slow oxidation processes of GR. Experimental conditions: [Fe(II)$_{GR}$] = 10 mM, [TBP] = 10 μM, and initial pH = 8.

while into magnetite and lepidocrocite after the slow oxidation reaction (Fig. 6a). The increase in oxidation rate could accelerate the transformation of oxidation products of GR from magnetite to lepidocrocite [46]. Therefore, Fe(II) was effectively preserved due to the formation of magnetite in the slow oxidation process while it was rapidly transformed into Fe(III) to form lepidocrocite in the fast oxidation process. The formation of magnetite with a stable crystallized structure is the key to the slow oxidation of Fe(II) and continuous activation of dioxygen, which has been demonstrated in our previous study [33]. Therefore, the slow oxidation process was more conducive to the continuous degradation of TBP.

EPR analysis was performed to verify the coexistence of H* and •OH in the GR-Pd(II) system under oxic conditions (Fig. 6b). EPR spectroscopy showed the signals attributed to HO$_2$• radical in the GR-Pd(II) system under oxic conditions, while no signal was detected in the GR alone. H* would react immediately with O$_2$ to produce HO$_2$• once O$_2$ was introduced [20]. The presence of HO$_2$• indicated the generation of H* in GR-Pd(II) system. HO$_2$• was known as the precursor of H$_2$O$_2$ and •OH, which could generate •OH via the O$_2$→HO$_2$•→H$_2$O$_2$→•OH pathway. In contrast, the pathway of dioxygen activation by GR alone was O$_2$→H$_2$O$_2$→•OH [32,33]. Therefore, the addition of Pd(II) altered the •OH generation pathway due to the involvement of H* . A weak HO$_2$• signal was also detected for GR-Pd(II) system under anoxic conditions due to the inevitable exposure of small amounts of oxygen during testing. This comparison also illustrated that the degree of oxygen participation could affect the signal strength of HO$_2$•. No characteristic peak of •OH was detected in the filtrate of GR-Pd(II) system by EPR, because the dioxygen activation by iron minerals, such as GR and magnetite, tends to produce surface-bound •OH rather than free •OH [47]. Therefore, the GR-Pd(II) system could co-produce H* and •OH under oxic conditions, while H* could also be involved in the reduction of DO to generate •OH. To further reveal the role of H* and •OH in the degradation of TBP, different concentration gradients of TBA were

added to the slow oxidation reaction system (Fig. 5d). It was found that the addition of TBA inhibited the reduction of TBP in the first 0.5 h, and the inhibition rate increased with increasing TBA concentrations. The reduction of TBP was not completely inhibited because part of the reduction process was achieved by direct electron transfer. On the other hand, the oxidative degradation of phenol at later stages was basically completely inhibited by TBA. It further demonstrated that the H* was responsible for the pre-reductive debromination of TBP and •OH was responsible for the post-oxidative degradation of phenol.

H* was not only the radical for the reduction of TBP, but that excess H* was also involved in the production of •OH. To further verify this hypothesis, •OH generation with different dosages of Pd(II) during the slow oxidation process was compared (Fig. 5e). When Pd(II) dosage was 20 μM and 40 μM, the production of •OH increased by 8.7% and 23.4% respectively compared with GR alone, indicating that the production of H* by a certain amount of Pd(II) was conducive to the generation of •OH. However, as the dosage of Pd(II) continued to increase, the production of •OH did not increase. The amount of •OH produced by 60 μM Pd(II) was equal to that by 20 μM Pd(II), and the amount of •OH decreased at 80 μM Pd(II), which might be because the production of H* increased with the increase of Pd-catalyzed sites while the production of •OH produced by GR was limited, too much H* would quench •OH. In addition, the intermediate reactive oxygen species H$_2$O$_2$ produced during the process of dioxygen activation by GR-Pd(II) was examined. Fig. 5f showed that H$_2$O$_2$ first increased and then decreased, and the H$_2$O$_2$ production in the GR-Pd(II) system was higher than that in the GR system. This result further indicated that excessive H* was beneficial to the reduction of O$_2$ to H$_2$O$_2$, which was further reduced by GR to form •OH. The degradation of TBP was also studied in GR-Pd(II) systems with different Pd(II) concentrations (Fig. S4a-b). The degradation process of TBP was basically the same with different dosages of Pd (II), i.e. TBP was rapidly reduced to phenol and phenol was then degraded by oxidation. In addition, phenol concentration decreased
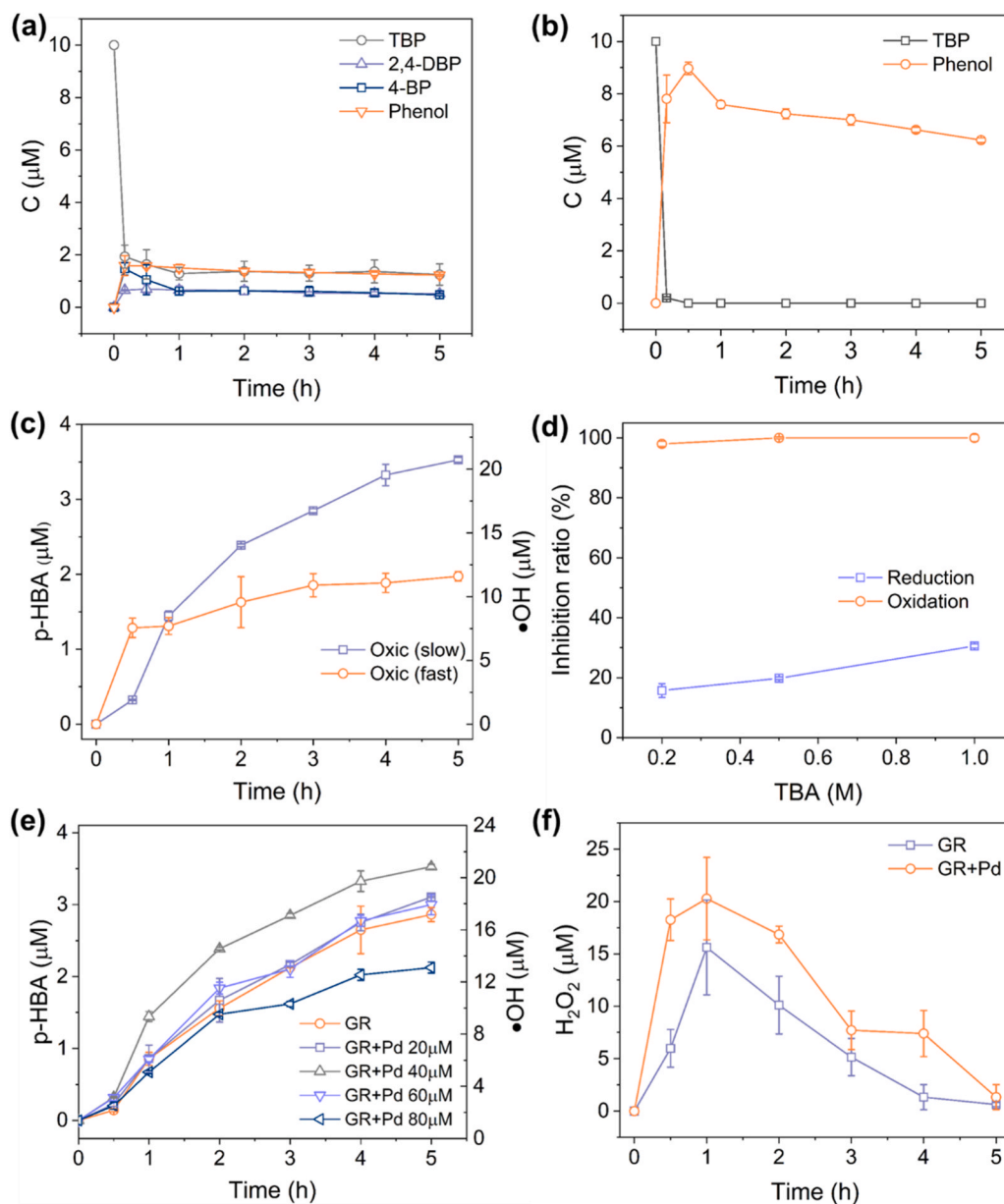
Fig. 5. The degradation of TBP and the production of intermediates by GR-Pd(II) in (a) fast and (b) slow oxidation processes. (c) Cumulative concentrations of •OH produced from GR-Pd(II) during fast and slow oxygenation. (d) The inhibition ratio of TBA on the reduction of TBP to phenol and oxidative degradation of phenol. (e) Effect of Pd(II) dosage on the production of •OH and (f) the production of H_2O_2 of GR and GR-Pd(II) in slow oxidation processes. Experimental conditions: $[Fe(II)_{GR}]$ = 10 mM, $[Pd(II)]$ = 40 μM except for (e), $[TBP]$ = 10 μM, and initial pH = 8.

with the increase of Pd(II) dosage but debromination rates were almost same (Fig. S4c). The reason that phenol was not completely detected at high concentrations of Pd(II) may be the adsorption of phenol at Pd(0) sites [48,49].

The debromination of TBP and the change of TOC under the single involvement and the synergistic involvement of H* and •OH were compared (Fig. 7c-d). During the slow oxidation of GR-Pd(II), TBP was rapidly reduced due to the intervention of H* . As a result, ∼28 μM of bromine ions were detected (Fig. 7c), completing 93% debromination. During the fast oxidation of GR-Pd(II), ∼15.1 μM of bromine ions were detected, completing 50.3% debromination. Although TBP did not achieve complete debromination in this process due to the early involvement of •OH, the synergistic involvement of H* and •OH greatly enhanced the debromination rate compared with the involvement of •OH alone in the GR system (Fig. 4c). In addition, TBP could not be mineralized by H* or •OH alone (Fig. 7d, Fig. 4d), but the synergistic

effect of H* and •OH realized the mineralization of TBP (Fig. 7d). The mineralization efficiency of TBP was 33% and 21% after the slow oxidation and fast oxidation process of GR-Pd(II) (Fig. 7d), indicating that the synergistic involvement of H* and •OH was crucial to achieve the mineralization of TBP. It was noteworthy that the first involvement of H* was favorable to the complete debromination and the final mineralization efficiency of TBP, while the synchronous involvement of H* and •OH would produce oxidation products that were not completely debrominated. Thus, the sequential reduction-oxidation process was more beneficial to the detoxification of TBP. In order to further verify the effect of the sequential involvement of H* and •OH, a rigorous reduction-to-oxidation experiment was carried out in the anoxic-to-oxic environment.
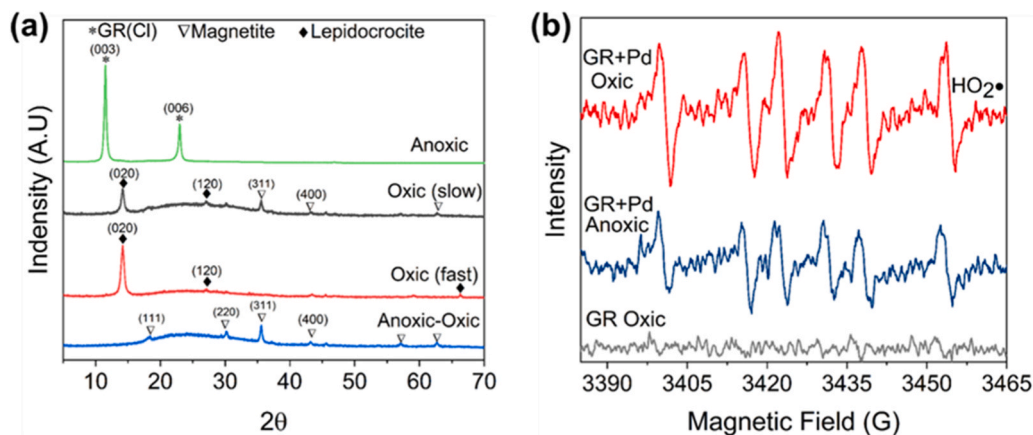
Fig. 6. (a) XRD patterns of GR-Pd(II) under different reaction conditions. (b) EPR spectra of GR and GR-Pd(II) under anoxic or oxic conditions.
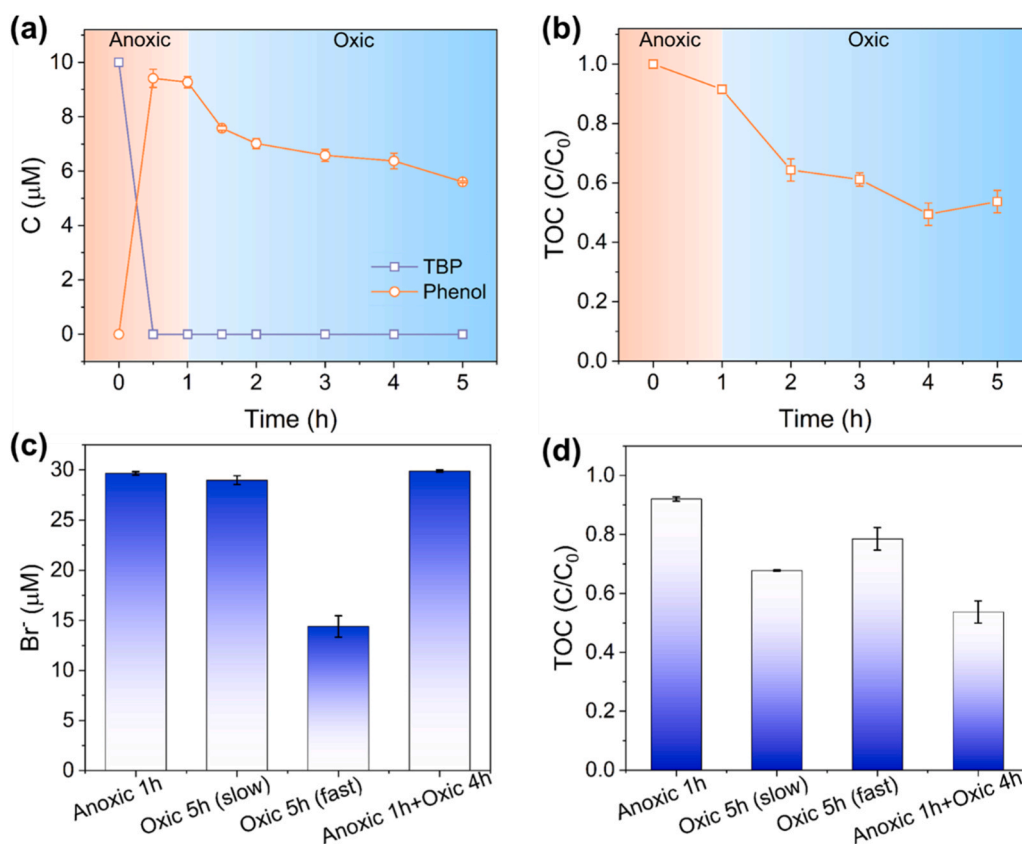

Fig. 7. (a) The degradation of TBP and (b) the change of TOC under anoxic-to-oxic transition conditions. (c) The production of Br⁻ and (d) the change of TOC in the GR-Pd(II) system under different conditions. Experimental conditions: $[Fe(II)]_{GR} = 10$ mM, $[Pd(II)] = 40$ μM, $[TBP] = 10$ μM, and initial pH = 8.

3.4. Degradation of TBP by sequential involvement of H* and •OH

3.4.1. Degradation of TBP in anoxic-to-oxic environment

In the process of anoxic 1 h -to-oxic 4 h, TBP was rapidly degraded to phenol within 0.5 h anoxic treatment (Fig. 7a). The concentrations of TBP and phenol basically remained unchanged from 0.5 h to 1 h, but decreased continuously in the subsequent 4 h of oxic treatment. The changes of debromination and TOC were monitored. TBP was completely debrominated (Fig. 7c), and TOC continued to decline under oxic conditions (Fig. 7b). The final mineralization efficiency reached 47% after 5 h of reaction, demonstrating that the sequential involvement of H* and •OH is more beneficial to the mineralization of TBP compared with the synchronous involvement of H* and •OH. Although

the slow oxidation under oxic conditions and the anoxic-to-oxic reaction of GR-Pd(II) both achieved the sequential reduction-oxidation of TBP by H* and •OH, the mineralization efficiency of TBP was different between the two processes. GR was gradually oxidized with the continuous infiltration of dioxygen during the slow oxidation process. However, under anoxic-to-oxic conditions, the characteristic peaks of GR were still detected by XRD after 1 h anoxic reaction and no other iron (hydr)oxides resulting from GR oxidation were observed (Fig. 6a). This indicated that the oxidation of GR by trace Pd(II) had no obvious effect on the structure of GR. Also, XPS data showed that the Fe(II) content of GR had little change in the first anoxic 1 h (Fig. 2a, Table S1). The Fe(II) consumption of GR during the pre-reduction process under anoxic-to-oxic conditions was less than that under oxic conditions, which was

responsible for a higher mineralization efficiency achieved by the anoxic-to-oxic sequential degradation process. Meanwhile, XPS showed that Pd(II) was also fully reduced to Pd(0) by GR, and the contents of both Fe(II) and Pd(0) after 1 h reaction under anoxic-to-oxic conditions were higher than those under oxic conditions, indicating that more active components were reserved for the following oxidation reaction. After 1 h anoxic and 4 h oxic reaction, the oxidation product of GR was magnetite, and no other iron minerals such as lepidocrocite were detected. Therefore, the sequential reduction-oxidation reaction was more favorable to the formation of magnetite, achieving continuous activation of dioxygen during oxic conditions.

3.4.2. Effects of Pd and GR dosages

TBP was completely reduced to phenol in the 0.5 h of anoxic reaction, and further degraded in the 1–5 h of oxic reaction with different dosages of Pd(II) (Fig. S5a). The amount of phenol decreased with the increase of Pd dosage, but the Br^- production with different Pd concentrations after 1 h anoxic reaction was almost 30 μM, demonstrating TBP was completely debrominated and further verified the adsorption of phenol at Pd(0) sites led to the decreased phenol concentration in reaction solution [48,49]. The effect of 2–30 mM GR on anoxic-to-oxic sequential degradation of TBP was also studied (Fig. S5b). The reduction of TBP to phenol was slowed down at low concentrations of GR. GR was the electron donor in the reaction, and the low dosage of GR would hinder the reduction of Pd(II) to Pd(0) together with the subsequent reductive debromination of TBP. It was also found that the high concentration of GR inhibited the oxidative degradation of phenol under oxic conditions. This was because high GR concentration
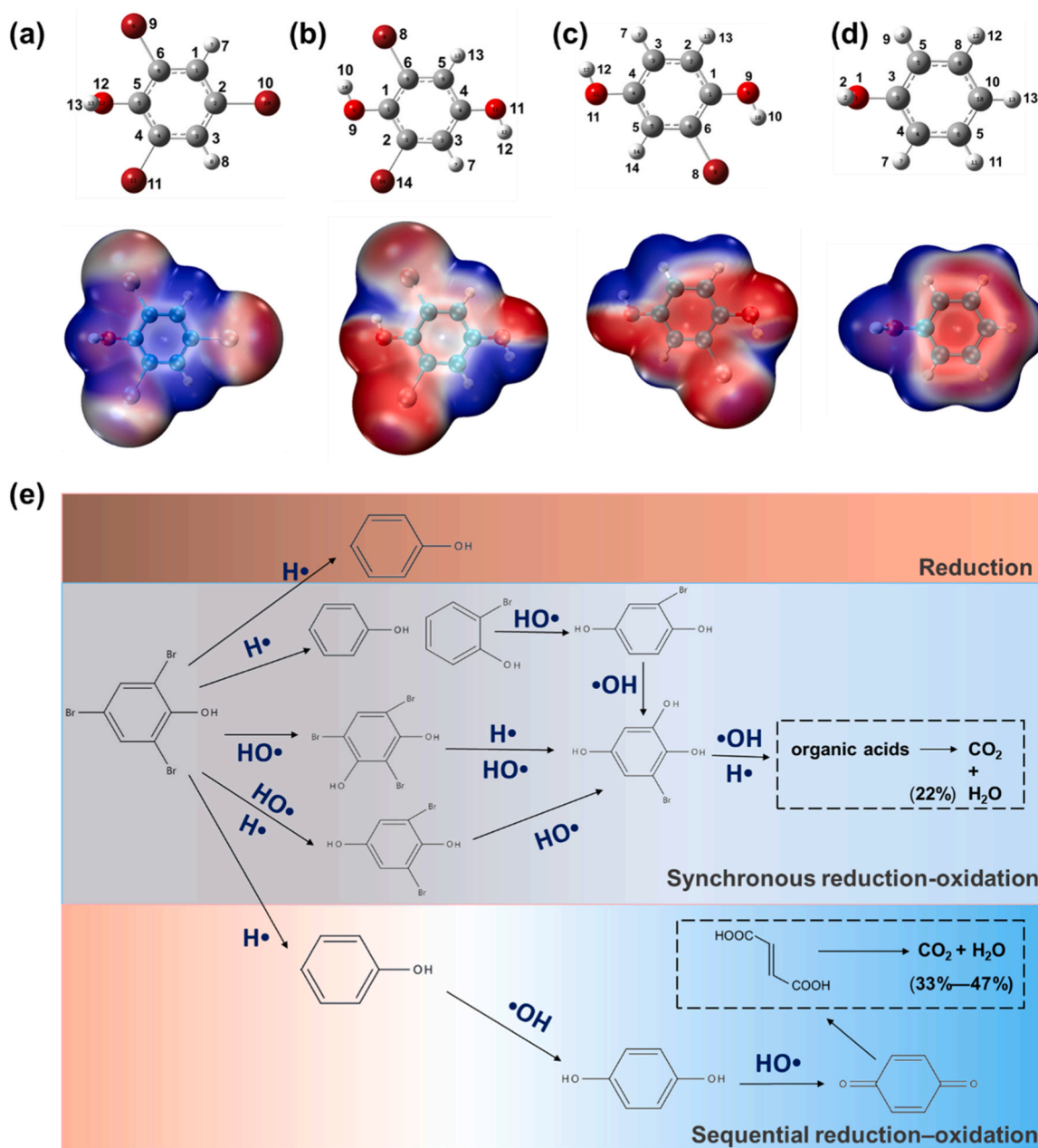

Fig. 8. Chemical structure (grey: carbon, red: oxygen, white: hydrogen, crimson: bromine) and ESP of (a) TBP, its oxidation products (b) dibromohydroquinone and (c) monobromohydroquinone, and its reduction product (d) phenol. The red and blue regions of ESP correspond to the most negative and positive ESP values, respectively. (e) Proposed debromination pathway of TBP by GR-Pd(II) during the reduction, synchronous reduction-oxidation and sequential reduction-oxidation process.

may quench the produced ●OH under oxic conditions, inhibiting the oxidative degradation of phenol.

3.5. Mechanisms of H* and ●OH intervention timing for TBP degradation

3.5.1. DFT calculation

In order to further reveal the importance of H* and ●OH intervention timing in the degradation of TBP, the DFT calculation of TBP and its oxidation/reduction products was performed. ESP can be used to explain and predict the electrostatic interaction between molecules [50–52]. The colors of the molecular electrostatic potential surface are defined as follows: blue regions indicate lack of electrons and vulnerability to nucleophilic attacks, white regions indicate neutral regions, and red regions indicate electron-rich regions and vulnerability to electrophilic attacks (Fig. 8). The incomplete debromination products with hydroxyl groups, such as dibromohydroquinone and monobromohydroquinone, were produced during the synchronous reduction-oxidation process of TBP. Compared with TBP, the hydroxylation process increases the negative potential of the uncleaved bromine atoms on the benzene ring (Fig. 8b-c), which makes incomplete debromination products difficult to undergo the nucleophilic attack of H* . As a result, these oxidation products with bromine were not completely debrominated by H* as quickly as TBP, which was the reason for the low debromination rate of TBP caused by synchronous effect of H* and ●OH during the rapid oxidation process. It is further confirmed that the first intervention of H* -involved reduction is the key to the complete debromination of TBP. In addition, the charge distribution of benzene ring of phenol, which is the complete debromination product of TBP, is dominated by electron-rich region (red) and almost no electron-deficient region (blue) (Fig. 8d). Therefore, the benzene ring is difficult to accept nucleophilic attack of H* , but is prone to become the chemical reaction site of electrophilic attack. Thus, phenol only underwent ring opening and further degradation under the attack of ●OH and could not be reduced by H* .

The Fukui index (f, f^+, f^0) is an effective method to gain insight into the region selectivity of the active species and is used to analyze nucleophilic, electrophilic and free radical reaction sites [53–55]. H* and ●OH belong to nucleophilic and electrophilic species, while ●OH could also cause free radical attacks. The f^+ values of the three bromine atoms Br10/Br11/Br12 in TBP are relatively high (Table S3), and these sites are readily attacked by electrons or H* . Therefore, the debromination reaction of TBP would occur rapidly under reducing conditions. Meanwhile, C1, C3 and Br10 of TBP have the highest f^0 value, and these sites are the most easily hydroxylated under the condition of synchronous redox treatment. Therefore, intermediate products such as tribromoresorcinol, dibromohydroquinone and monobromohydroquinone are formed under the synchronous effect of H* and ●OH. In addition, the C3 and C5 of dibromohydroquinone sites would undergo further hydroxylation due to their high f^0 (Table S4). The C1, O9, C4, and O11 of monobromobenzenediol are the most active electrophilic reaction sites (Table S5). The C1-O9 and C4-O11 bonds could be cleaved by subsequent ●OH attack, resulting in the eventual mineralization of TBP into H_2O and CO_2. During the sequential reduction-oxidation process, the reduction product phenol is readily oxidized to p-phenol by hydroxylation of the para-aromatic ring due to the highest f^0 value of C10 (Table S6), which is followed by further cleavage or ring opening.

3.5.2. Degradation pathway

According to theoretical calculation and LC-MS results (Fig. S6), we compared the degradation pathways of TBP in the reduction process with only H* , synchronous and sequential redox process with coexistence of H* and ●OH (Fig. 8e). TBP was only reduced to phenol without further degradation in the reduction process with only H* . According to our previous study, only oxidation products with bromine were produced [33], and TBP was not mineralized in the oxidation process with only ●OH. However, in the process of synergetic degradation of TBP by

H* and ●OH, the reduction, oxidation products and the decrease of TOC were observed. Based on LC-MS and TOC analysis, the possible degradation pathways of TBP during the synchronous involvement of H* and ●OH were proposed: in the first stage, H* and ●OH simultaneously attack the C-Br bond and C-H bond of TBP, leading to hydroxylation and debromination of aromatic rings and the formation of phenolic intermediates such as dibromohydroquinone and monobromohydroquinone. In the second stage, ring-opening occurred due to further attack of polyhydroxyl compound products by ●OH and a series of short-chain carboxylic acids were produced. The carboxylic acid products were degraded by the further attack of H* and ●OH and eventually converted to Br^-, H_2O, and CO_2. Therefore, the mineralization of tribromophenol was realized under the synchronous involvement of H* and ●OH. By contrast, in the process of sequential reduction and oxidation, TBP was firstly rapidly reduced to phenol by H* , and then phenol was hydroxylated to p-phenol under the attack of ●OH in the oxic environment. The p-phenol was further oxidized to the benzoquinone (Fig. S6c), followed by the ring-opening to produce small-molecular acids and mineralized into H_2O and CO_2 eventually. After the sequential attack of H* and ●OH, a higher mineralization efficiency of TBP was achieved. Through the above degradation pathways, it was found that the sequence of redox reactions initiated by H* and OH could change the intermediates of TBP. In the synchronous reduction-oxidation process, incomplete debromination intermediates were produced due to the involvement of ●OH in the debromination process of TBP. These hydroxylated incomplete debromination products are less likely to be attacked by H* for reduction compared with TBP, and more difficult to be completely mineralized by ●OH compared with phenol. Therefore, the mineralization efficiency of TBP is lower under the synchronous involvement of H* and ●OH than under the sequential involvement.

The detailed reaction pathways during the synchronous and sequential reduction-oxidation process were listed in Fig. S7 and the geometries of reactants were optimized via DFT (Fig. S8). The detailed information of transition state geometries, including three-dimensional coordinates, charge, spin-multiplicity and the value of imaginary frequency, was provided in Table S7. Furthermore, the geometries were examined using intrinsic reaction coordinate (IRC) which also could see how the molecule had changed before and after the reaction [56]. The calculation results of IRC confirmed the reactants and products connected in transition state, which were consistent with the reaction pathway in Fig. S7, and further confirmed the accuracy of the reaction pathway. In addition, the energy diagrams corresponding to different transition state geometries (in Gaussview visual interface) clearly showed the energy changes in the chemical reaction process. The free energy for TBP degradation of each reaction step was calculated (Fig. S9). The low reaction energy barriers were observed in both sequential and synchronous reaction pathways, which was the reason for the continuous degradation of TBP by synergistic involvement of H* and ●OH. It further proved that our experiment could achieve efficient degradation of TBP without external energy input. Fig. S10 depicts the optimal geometries and electron spin density maps of TBP and its important intermediates after adding or losing one electron. After adding and losing one electron, the highest electron density sites of these reactants are on the Br atom and the C atom of benzene ring respectively, indicating that these sites are unstable and easily become the next reaction sites. Hence, it can be inferred that H* is beneficial to initiate the debromination reaction while ●OH is beneficial to the initiate benzene ring opening reaction, which conforms with our experimental results. Fig. S11a reflects the spin density of the transition state configurations obtained by H* or ●OH attacking TBP and its intermediates. It can be seen that under transition state, the H atom, Br atom or OH group of the reactants and the free radicals have opposite spins and are easy to combine into bonds [57]. Besides, after the attack of free radicals, the largest atomic spin density was found at the C atom deprived of an H atom, Br atom or OH group (Fig. S11b), demonstrating that unpaired electrons become more active on electronic orbital and

these carbon sites were prone to react under the further attack by free radicals. The above theoretical calculation further confirmed the feasibility of the TBP degradation pathway in the redox reaction by H* and ●OH.

3.6. TBP degradation in long-term reaction

The long-term removal efficiency of TBP by GR-Pd (II) under different conditions was also investigated. As shown in Fig. S12a, the phenol generated from the reduction of TBP by GR-Pd(II) was not further degraded in the long-term anoxic reaction, which confirmed that GR-Pd (II) had no reducing capability for phenol. TBP or its degradation products could be further degraded in the long-term fast oxidation, slow oxidation and anoxic-to-oxic transition process (Fig. S12b-d), but the degradation rate was very slow in the late stage (5–72 h), indicating that the catalytic activity of GR was weakened along the oxidation process. Also, TOC results showed that the final mineralization efficiency reached 30%, 41% and 50% after 72 h of fast oxidation, slow oxidation and anoxic-to-oxic transition reaction respectively, which was slightly higher than that of short-term reaction.

4. Environmental significance

GR is an iron(II)-bearing mineral usually found in an oxygen-deficient and iron-rich subsurface environment. Trace amounts of Pd^{2+} ions mixed with GR produce highly reductive radicals H* , which can rapidly debrominate TBP completely. The anoxic subsurface environments are often disturbed by natural processes and human activities. Such disturbances can introduce dioxygen and change redox conditions of groundwater. Even in oxic conditions, GR-Pd(II) still has reduction effect on TBP. Once dioxygen is introduced, H* and ●OH are produced by the GR-Pd(II) system and the synergistic involvement of H* and ●OH can realize the mineralization of TBP, which is beneficial for the complete detoxification of TBP. Noticeably, the rate and timing of dioxygen entry into groundwater directly affect the intervention sequence of H* and ●OH. The slow oxidation or anoxic-to-oxic transition conditions could lead to the sequential involvement of H* and ●OH for TBP degradation, which achieved high mineralization efficiency of TBP. This study provides guidance on the remediation of TBP-contaminated groundwater in Fe(II)-rich redox-fluctuating subsurface environment.

5. Conclusion

In this study, we developed a synergetic reduction-oxidation system using GR-Pd(II), in which H* and ●OH coexisted in the system and synergistically degraded TBP. The experiment-setup was simple and did not require additional energy input, which was an advantage compared with the previous electrocatalytic or photoelectrocatalytic experiments. Furthermore, it is difficult to achieve complete debromination or mineralization of TBP in previous electrocatalytic and photocatalytic systems (Table S8), our study could realize complete debromination and mineralization of TBP by regulating intervention timing of H* or ●OH. The Pd(0) produced by the reduction of Pd(II) by GR is the catalytic site for H* generation, and the excess H* also promotes the generation of ●OH when dioxygen is introduced. More importantly, the reaction mechanism between GR-Pd(II) with TBP could be selectively regulated by controlling the reaction environment. The diffusion rate of dioxygen into reaction solution determines the intervention timing of ●OH. Both the synchronous and sequential involvement of H* and ●OH could realize the mineralization of TBP, which was impossible for the single involvement of H* or ●OH. However, the initiation sequence of redox reaction by H* and ●OH directly affected the degradation pathway of TBP. The most efficient way of TBP mineralization is that H* firstly initiates the reductive debromination reaction and ●OH further attacks the reduction product phenol. The study clearly confirms that the synergistic redox reaction and the involvement timing of H* and ●OH are

crucial for the efficient mineralization of TBP.

CRediT authorship contribution statement

Xuejie Zhang: Investigation, Data curation, Writing – original draft. **Qianqian Jia**: Visualization, Investigation. **Jia Deng**: Software, Validation. **Lili Li**: Supervision, Validation. **Yitao Dai**: Supervision. **Liandong Zhu**: Supervision. **Li-Zhi Huang**: Conceptualization, Supervision, Validation, Writing – review & editing.

Declaration of Competing Interest

The authors declare that they have no known competing financial interests or personal relationships that could have appeared to influence the work reported in this paper.

Data Availability

Data will be made available on request.

Acknowledgements

Appendix A. Supporting information

Supplementary data associated with this article can be found in the online version at doi:10.1016/j.apcatb.2023.123510.

References

[1] J. Deng, E.L. Gao, F. Wu, Z.X. You, X.Z. Li, S.X. Gao, L.Z. Huang, Generation of atomic hydrogen by Ni-Fe hydroxides: mechanism and activity for hydrodechlorination of trichloroethylene, Water Res. 207 (2021), https://doi.org/10.1016/j.watres.2021.117802.

[2] B. Liu, H. Zhang, Q. Lu, G.H. Li, F. Zhang, A Cu-Ni bimetallic cathode with nanostructured copper array for enhanced hydrodechlorination of trichloroethylene (TCE), Sci. Total Environ. 635 (2018) 1417–1425, https://doi.org/10.1016/j.scitotenv.2018.04.238.

[3] C.L. Yu, Y.T. Zhang, Y.X. Lu, A. Qian, P. Zhang, Y.P. Cui, S.H. Yuan, Mechanistic insight into humic acid-enhanced hydroxyl radical production from Fe(II)-bearing clay mineral oxygenation, Environ. Sci. Technol. 55 (2021) 13366–13375, https://doi.org/10.1021/acs.est.1c02461.

[4] G.H. Yu, Y. Kuzyakov, Fenton chemistry and reactive oxygen species in soil: abiotic mechanisms of biotic processes, controls and consequences for carbon and nutrient cycling, Earth-Sci. Rev. 214 (2021), https://doi.org/10.1016/j.earscirev.2021.103525.

[5] G.K. Parshetti, R.A. Doong, Dechlorination of trichloroethylene by Ni/Fe nanoparticles immobilized in PEG/PVDF and PEG/nylon 66 membranes, Water Res. 43 (2009) 3086–3094, https://doi.org/10.1016/j.watres.2009.04.037.

[6] X.Y. Wang, C. Chen, H.L. Liu, J. Ma, Preparation and characterization of PAA/PVDF membrane-immobilized Pd/Fe nanoparticles for dechlorination of trichloroacetic acid, Water Res. 42 (2008) 4656–4664, https://doi.org/10.1016/j.watres.2008.08.005.

[7] H.W. Wu, Q.Y. Feng, Fabrication of bimetallic Ag/Fe immobilized on modified biochar for removal of carbon tetrachloride, J. Environ. Sci. 54 (2017) 346–357, https://doi.org/10.1016/j.jes.2016.11.017.

[8] A.Z. Li, X. Zhao, Y.N. Hou, H.J. Liu, L.Y. Wu, J.H. Qu, The electrocatalytic dechlorination of chloroacetic acids at electrodeposited Pd/Fe-modified carbon paper electrode, Appl. Catal. B-Environ. 111 (2012) 628–635, https://doi.org/10.1016/j.apcatb.2011.11.016.

[9] R. Mao, N. Li, H.C. Lan, X. Zhao, H.J. Liu, J.H. Qu, M. Sun, Dechlorination of trichloroacetic acid using a noble metal-free graphene-Cu foam electrode via direct cathodic reduction and atomic H, Environ. Sci. Technol. 50 (2016) 3829–3837, https://doi.org/10.1021/acs.est.5b05006.

[10] G.M. Jiang, M.N. Lan, Z.Y. Zhang, X.S. Lv, Z.M. Lou, X.H. Xu, F. Dong, S. Zhang, Identification of active hydrogen species on palladium nanoparticles for an

enhanced electrocatalytic hydrodechlorination of 2,4-Dichlorophenol in water, Environ. Sci. Technol. 51 (2017) 7599–7605, https://doi.org/10.1021/acs.est.7b01128.

[11] F.Y. Xu, S.B. Deng, J. Xu, W. Zhang, M. Wu, B. Wang, J. Huang, G. Yu, Highly active and stable Ni-Fe bimetal prepared by ball milling for catalytic hydrodechlorination of 4-chlorophenol, Environ. Sci. Technol. 46 (2012) 4576–4582, https://doi.org/10.1021/es203876e.

[12] J.V. Goldstone, M.J. Pullin, S. Bertilsson, B.M. Voelker, Reactions of hydroxyl radical with humic substances: bleaching, mineralization, and production of bioavailable carbon substrates, Environ. Sci. Technol. 36 (2002) 364–372, https://doi.org/10.1021/es0109646.

[13] K. Mopper, X.L. Zhou, Hydroxyl radical photoproduction in the sea and its potential impact on marine, Science 250 (1990) 661–664, https://doi.org/10.1126/science.250.4981.661.

[14] S.E. Page, J.R. Logan, R.M. Cory, K. McNeill, Evidence for dissolved organic matter as the primary source and sink of photochemically produced hydroxyl radical in arctic surface waters, Environ. Sci. -Process. Impacts 16 (2014) 807–822, https://doi.org/10.1039/c3em00596h.

[15] G.D. Gao, Q.Y. Zhang, Z.W. Hao, C.D. Vecitis, Carbon nanotube membrane stack for flow-through sequential regenerative electro-fenton, Environ. Sci. Technol. 49 (2015) 2375–2383, https://doi.org/10.1021/es505679e.

[16] R. Mao, H.C. Lan, L. Yan, X. Zhao, H.J. Liu, J.H. Qu, Enhanced indirect atomic H* reduction at a hybrid Pd/graphene cathode for electrochemical dechlorination under low negative potentials, Environ. Sci. -Nano 5 (2018) 2282–2292, https://doi.org/10.1039/c8en00727f.

[17] R. Mao, X. Zhao, H.C. Lan, H.J. Liu, J.H. Qu, Graphene-modified Pd/C cathode and Pd/GAC particles for enhanced electrocatalytic removal of bromate in a continuous three-dimensional electrochemical reactor, Water Res. 77 (2015) 1–12, https://doi.org/10.1016/j.watres.2015.03.002.

[18] J. Zhang, Q.H. Ji, H.C. Lan, G. Zhang, H.J. Liu, J.H. Qu, Synchronous reduction-oxidation process for efficient removal of trichloroacetic acid: H* initiates dechlorination and center dot OH is responsible for removal efficiency, Environ. Sci. Technol. 53 (2019) 14586–14594, https://doi.org/10.1021/acs.est.9b05389.

[19] J. Zhang, G. Zhang, H.C. Lan, J.H. Qu, H.J. Liu, Synergetic hydroxyl radical oxidation with atomic hydrogen reduction lowers the organochlorine conversion barrier and potentiates effective contaminant mineralization, Environ. Sci. Technol. 55 (2021) 3296–3304, https://doi.org/10.1021/acs.est.0c07271.

[20] P.C. Guo, C.W. Yang, Z.Q. Chu, X. Zhang, G.P. Sheng, Synchronous reduction-oxidation of 2,4,6-tribromophenol using bifunctional AgPd@CDs in a three dimensional electrochemical reactor, Appl. Catal. B-Environ. 297 (2021), https://doi.org/10.1016/j.apcatb.2021.120467.

[21] R.L. Smith, R.W. Harvey, Importance of closely spaced vertical sampling in delineating chemical and microbiological gradients in groundwater studies, J. Contam. Hydrol. 7 (1991) 285–300, https://doi.org/10.1016/0169-7722(91)90032-V.

[22] W.F. Chen, T.K. Liu, Dissolved oxygen and nitrate of groundwater in Choshui Fan-Delta, western Taiwan, Environ. Geol. 44 (2003) 731–737, https://doi.org/10.1007/s00254-003-0823-0.

[23] T. Datry, F. Malard, J. Gibert, Dynamics of solutes and dissolved oxygen in shallow urban groundwater below a stormwater infiltration basin, Sci. Total Environ. 329 (2004) 215–229, https://doi.org/10.1016/j.scitotenv.2004.02.022.

[24] S. Chakraborty, B. Nath, D. Chatterjee, L. Charlet, Retardation of arsenic transport by oxidized Holocene aquifer sediments of West Bengal, India, J. Hydrol. 518 (2014) 460–463, https://doi.org/10.1016/j.jhydrol.2013.07.028.

[25] B.C. Christiansen, T. Balic-Zunic, K. Dideriksen, S.L.S. Stipp, Identification of green rust in groundwater, Geochim. Et. Cosmochim. Acta 73 (2009), https://doi.org/10.1021/es8011047.

[26] J.M.R. Genin, G. Bourrie, F. Trolard, M. Abdelmoula, A. Jaffrezic, P. Refait, V. Maitre, B. Humbert, A. Herbillon, Thermodynamic equilibria in aqueous suspensions of synthetic and natural Fe(II)-Fe(III) green rusts: occurrences of the mineral in hydromorphic soils, Environ. Sci. Technol. 32 (1998) 1058–1068, https://doi.org/10.1021/es970547m.

[27] L.Z. Huang, Z. Yin, N.G.A. Cooper, W.Z. Yin, E.T. Bjerglund, B.W. Strobel, H.C. B. Hansen, Copper-mediated reductive dechlorination by green rust intercalated with dodecanoate, J. Hazard. Mater. 345 (2018) 18–26, https://doi.org/10.1016/j.jhazmat.2017.11.011.

[28] E.J. O'Loughlin, K.M. Kemner, D.R. Burris, Effects of Ag-I, Au-III, and Cu-II on the reductive dechlorination of carbon tetrachloride by green rust, Environ. Sci. Technol. 37 (2003) 2905–2912, https://doi.org/10.1021/es030304w.

[29] B.P. Chaplin, M. Reinhard, W.F. Schneider, C. Schuth, J.R. Shapley, T. J. Strathmann, C.J. Werth, Critical review of Pd-based catalytic treatment of priority contaminants in water, Environ. Sci. Technol. 46 (2012) 3655–3670, https://doi.org/10.1021/es204087q.

[30] B. Yang, G. Yu, J. Huang, Electrocatalytic hydrodechlorination of 2,4,5-trichloro-biphenyl on a palladium-modified nickel foam cathode, Environ. Sci. Technol. 41 (2007) 7503–7508, https://doi.org/10.1021/es071168o.

[31] L. Fang, L. Xu, J. Deng, S. Gao, L.-Z. Huang, Induced generation of hydroxyl radicals from green rust under oxic conditions by iron-phosphate complexes, Chem. Eng. J. 414 (2021), https://doi.org/10.1016/j.cej.2021.128780.

[32] X. Zhang, J. Deng, Q. Jia, B. Ji, Y. Dai, L.-Z. Huang, Mineralization of tribromophenol under anoxic/oxic conditions in the presence of copper(II) doped green rust: importance of sequential reduction-oxidation process, Water Res. 222 (2022), https://doi.org/10.1016/j.watres.2022.118959.

[33] X.J. Zhang, Q.Q. Jia, J. Deng, F. Wu, L.Z. Huang, Interaction between green rust and tribromophenol under anoxic, oxic and anoxic-to-oxic conditions: adsorption,

[34] Z. Ronen, S. Visnovsky, A. Nejidat, Soil extracts and co-culture assist biodegradation of 2,4,6-tribromophenol in culture and soil by an auxotrophic achromobacter piechaudii strain TBPZ, Soil Biol. Biochem. 37 (2005) 1640–1647, https://doi.org/10.1016/j.soilbio.2005.02.001.

[35] W.J. Sim, S.H. Lee, I.S. Lee, S.D. Choi, J.E. Oh, Distribution and formation of chlorophenols and bromophenols in marine and riverine environments, Chemosphere 77 (2009) 552–558, https://doi.org/10.1016/j.chemosphere.2009.07.006.

[36] L. Zu, G. Li, J. An, J. Li, T. An, Kinetic optimization of biodegradation and debromination of 2,4,6-tribromophenol using response surface methodology, Int. Biodeterior. Biodegrad. 76 (2013) 18–23, https://doi.org/10.1016/j.ibiod.2012.06.014.

[37] T. Yamada, Y. Takahama, Y. Yamada, Biodegradation of 2,4,6-tribromophenol by Ochrobactrum sp strain TB01, Biosci. Biotechnol. Biochem. 72 (2008) 1264–1271, https://doi.org/10.1271/bbb.70755.

[38] W. Yin, L. Huang, E.B. Pedersen, C. Frandsen, H.C.B. Hansen, Glycine buffered synthesis of layered iron(II)-iron(III) hydroxides (green rusts), J. Colloid Interface Sci. 497 (2017) 429–438, https://doi.org/10.1016/j.jcis.2016.11.076.

[39] L.-Z. Huang, K.B. Ayala-Luis, L. Fang, K.N. Dalby, T. Kasama, C.B. Koch, H.C. B. Hansen, Oxidation of dodecanoate intercalated Iron(II)-Iron(III) layered double hydroxide to form 2D Iron(III) (Hydr)oxide layers, Eur. J. Inorg. Chem. 2013 (2013) 5718–5727, https://doi.org/10.1002/ejic.201300735.

[40] S. Peulon, L. Legrand, H. Antony, A. Chausse, Electrochemical deposition of thin films of green rusts 1 and 2 on inert gold substrate, Electrochem. Commun. 5 (2003) 208–213, https://doi.org/10.1016/s1388-2481(03)00019-5.

[41] F. Trolard, J.M.R. Genin, M. Abdelmoula, G. Bourrie, B. Humbert, A. Herbillon, Identification of a green rust mineral in a reductomorphic soil by Mossbauer and Raman spectroscopies, Geochim. Et. Cosmochim. Acta 61 (1997) 1107–1111, https://doi.org/10.1016/s0016-7037(96)00381-x.

[42] S. Das, M.J. Hendry, Application of Raman spectroscopy to identify iron minerals commonly found in mine wastes, Chem. Geol. 290 (2011) 101–108, https://doi.org/10.1016/j.chemgeo.2011.09.001.

[43] H.P. Rong, S.F. Cai, Z.Q. Niu, Y.D. Li, Composition-dependent catalytic activity of bimetallic nanocrystals: AgPd-catalyzed hydrodechlorination of 4-Chlorophenol, Acs Catal. 3 (2013) 1560–1563, https://doi.org/10.1021/cs400282a.

[44] L.Z. Huang, X.J. Zhang, R. Liu, L.P. Fang, The redox chemistry of phosphate complexed green rusts: Limited oxidative transformation and phosphate release, Chem. Eng. J. 429 (2022), https://doi.org/10.1016/j.cej.2021.132417.

[45] X.M. Wang, F. Liu, W.F. Tan, X.H. Feng, L.K. Koopal, Transformation of hydroxycarbonate green rust into crystalline iron (hydr)oxides: Influences of reaction conditions and underlying mechanisms, Chem. Geol. 351 (2013) 57–65, https://doi.org/10.1016/j.chemgeo.2013.05.003.

[46] J.M.R. Genin, C. Ruby, A. Gehin, P. Refait, Synthesis of green rusts by oxidation of Fe(OH)$_2$, their products of oxidation and reduction of ferric oxyhydroxides; Eh-pH Pourbaix diagrams, Comptes Rendus Geosci. 338 (2006) 433–446, https://doi.org/10.1016/j.crte.2006.04.004.

[47] L.L. Wang, H.Y. Du, H.C. Xu, H. Li, L.A. Li, Insights into phenanthrene attenuation by hydroxyl radicals from reduced iron-bearing mineral oxygenation, J. Hazard. Mater. 439 (2022), https://doi.org/10.1016/j.jhazmat.2022.129658.

[48] Y.H. Liu, F.L. Yang, P.L. Yue, G.H. Chen, Catalytic dechlorination of chlorophenols in water by palladium/iron, Water Res. 35 (2001) 1887–1890, https://doi.org/10.1016/s0043-1354(00)00463-2.

[49] A.J.R. Hensley, Y. Wang, J.S. McEwen, Adsorption of phenol on Fe (110) and Pd (111) from first principles, Surf. Sci. 630 (2014) 244–253, https://doi.org/10.1016/j.susc.2014.08.003.

[50] H. Boulebd, Theoretical insights into the antioxidant activity of moracin T, Free Radic. Res. 54 (2020) 221–230, https://doi.org/10.1080/10715762.2020.1747616.

[51] C.J. Li, Y.H. Zhang, W. Cai, X.J. Zhang, Y.F. Xie, Y.H. Guo, H. Yu, W.R. Yao, H. Qian, Mechanism insights into the transformation of carbosulfan during apple drying processes, Ecotoxicol. Environ. Saf. 201 (2020), https://doi.org/10.1016/j.ecoenv.2020.110729.

[52] M.M. Feng, R.H. Zeng, S.L. Chou, F.L. Gu, Enhancing the understanding of the redox properties of lithium-inserted anthraquinone derivatives by regulating molecular structure, J. Electroanal. Chem. 887 (2021), https://doi.org/10.1016/j.jelechem.2021.115172.

[53] W. Liu, Y.Y. Li, F.Y. Liu, W. Jiang, D.D. Zhang, J.L. Liang, Visible-light-driven photocatalytic degradation of diclofenac by carbon quantum dots modified porous g-C3N4: mechanisms, degradation pathway and DFT calculation, Water Res. 151 (2019) 8–19, https://doi.org/10.1016/j.watres.2018.11.084.

[54] D.D. Zhang, J.J. Qi, H.D. Ji, S. Li, L. Chen, T.B. Huang, C.K. Xu, X.M. Chen, W. Liu, Photocatalytic degradation of ofloxacin by perovskite-type NaNbO3 nanorods modified g-C3N4 heterojunction under simulated solar light: theoretical calculation, ofloxacin degradation pathways and toxicity evolution, Chem. Eng. J. 400 (2020), https://doi.org/10.1016/j.cej.2020.125918.

[55] X. Gao, J. Chen, H.N. Che, Y.H. Ao, P.F. Wang, Rationally constructing of a novel composite photocatalyst with multi charge transfer channels for highly efficient sulfamethoxazole elimination: mechanism, degradation pathway and DFT

calculation, Chem. Eng. J. 426 (2021), https://doi.org/10.1016/j. cej.2021.131585.

[56] S. Erdogan, D. Isin, A DFT study on OH radical scavenging activities of eriodictyol, Isosakuranetin and pinocembrin, J. Biomol. Struct. Dyn. 40 (2022) 10802–10811, https://doi.org/10.1080/07391102.2021.1950572.

[57] R.F.W. Bader, A bond path: a universal indicator of bonded interactions, J. Phys. Chem. A 102 (1998) 7314–7323, https://doi.org/10.1021/jp981794v.